PERGAMON

International Journal of Multiphase Flow 26 (2000) 99–123

International Journal of Multiphase Flow

www.elsevier.com/locate/ijmulflow

Modelling two-phase equilibrium in three-dimensional porous microstructures

F.S. Magnani [1], P.C. Philippi*, Z.R. Liang, C.P. Fernandes

Mechanical Engineering Department, Federal University of Santa Catarina, Cx. P. 476, 88040-900, Florianópolis SC, Brazil

Received 11 February 1998; received in revised form 13 January 1999

Abstract

This work presents a methodology for determining the interface between wetting and non-wetting phases inside a three-dimensional (3D) porous space at a given equilibrium state. The work is limited to the study of mechanical equilibrium. Mass transfer between different phases is not considered. The method is based on a 3D extension of the opening method from image analysis, applied on 3D stochastically reconstructed porous microstructures. The advantage of the presently proposed methodology with respect to percolation networks conception is that simplifying assumptions regarding the geometry of the porous space are not required. In fact, invasion of wetting fluid into a real porous structure in imbibition and wetting fluid retention at the later stages of drainage occur spatially through a complex structure of corners and intrinsic irregularities of pore surfaces that are very difficult to model by using percolation networks. Simulation results were compared with experimental data related to mercury intrusion and water–oil capillary curves for a Berea sandstone.

Keywords: Two-phase mechanical equilibrium; Three-dimensional porous structures

1. Introduction

The problem of predicting macroscopic transport properties from the underlying microscopic structure and pore-scale physics has been the subject of extensive investigation in recent years.

* Corresponding author.

[1] Presently at Mechanical Engineering Department of Federal University of Pernambuco, 50740-530, Recife PE, Brasil.

0301-9322/00/$ - see front matter
PII: S0301-9322(99)00008-7

Retention and transfer of fluids in porous structures is, presently, conceived starting from two basic conceptions. In the first one, porous space is considered as a discrete set of constrictions and cavities connected between themselves in a percolation network. In the second one, porous structure is reconstructed in three dimensions by conserving the first moments of the phase function, trying to match more closely to the geometry of real media and enabling one to create numerical realizations of the sample with the desired geometric properties. Advanced techniques such as microtomography (Hazlett, 1995; Spanne et al., 1994) and serial sectioning (Koplik et al., 1984; Kwiecien et al., 1990) could provide a detailed description of the 3D pore structures of porous materials. These techniques are, however, of low resolution, expensive and/or not readily available.

In the first and, also, the oldest conception, microscopic models are frequently, monodisperse models, based on random percolation networks of sites and/or bonds, interacting between themselves in a single scale. Classically, sites are randomly distributed in a network, with a constant or variable coordination number, which is the number of sites that are neighbours of each site in the network, Philippi and Souza (1995). The size of the bond connecting each two contiguous sites is randomly chosen so as to remain smaller than the size of the connected sites. Several well-known problems are associated with this reconstruction procedure: (i) it is very difficult to choose a particular constant coordination number Z for the porous structure or to ascertain a realistic distribution law for this parameter, (ii) it is very difficult to access the size distribution of constrictions and (iii) for simplicity reasons, networks are frequently, spatially non-correlated. Mercury intrusion and sorption isotherms have been used to estimate the size distribution of constrictions (Chatzis and Dullien, 1982; Daïan and Saliba, 1991). In general, several parameters models are needed in this kind of work, which are adjusted to fit the model to experimental data. In fact, the introduction of bonds in the percolation system is, frequently, a necessary hypothesis in percolation models, due to the lack of information about the spatial distribution of pores. Chatzis and Dullien (1982) and Daïan and Saliba (1991) use a local correlation between throat size and pore size given by a relationship between the cumulative distributions of throats and pores. Mayagoitia et al. (1989) have also considered a local correlation between a site and the contiguous bond, generated by the conditional probability related to the impossibility of connecting a site with a bond greater in size. Spatially correlated networks of sites and bonds were considered, e.g., by Renault (1991), to study the influence of spatial correlation on the percolation threshold and by Ioannids and Chatzis (1993a, 1993b) and Tsakiroglou and Payatakes (1992) to study the effect of spatial correlation on mercury intrusion. In recent years pore bodies and throats have been simulated using prisms of rectangular cross-section for describing wetting fluid corner invasion and the later stages of pore filling during drainage (Ioannidis and Chatzis, 1993c). This kind of hypothesis, introduced by Lenormand (1981), is necessary for correctly describing non-wetting fluid trapping, which is a fundamental physical process in oil recovery technology.

The second and more recent conception has been developed following the introduction of enhanced image analysis methods used over pictures of highly polished surfaces of porous materials, taken with optical or electron scanning microscopes (Adler, 1992; Philippi et al., 1994; Pieritz and Philippi, 1995; Laurent and Frendo-Rosso, 1992; Fernandes, 1994). The

information on porous medium is obtained following a sequence of image analysis operations consisting in image acquisition, segmentation and morphology analysis of the structure. Three-dimensional reconstruction of the porous structure conserves, usually, the porosity and auto-correlation function measured on a binary image obtained from these pictures. Joshi (1974), Quiblier (1984), Adler et al. (1990) and Fernandes (1994) have extensively studied this operation. This method has been applied to the prediction of important petrophysical and reservoir engineering properties, such as permeability (Adler et al. 1990) and formation factor (Ioannidis et al. 1995) with reasonable success. Thovert et al. (1993) used the reconstructed porous media and developed thinning algorithms to obtain the graph of the 3D pore structure. The topological characteristics were derived. Nowadays, results are restricted to single-phase flow: the flow problem is solved inside a *known* geometrical domain, which is the *whole* porous space.

Recently, a photoluminescent volumetric imaging method, with a micronic spatial resolution, was used by Montemagno and Gray (1995) to experimentally determine *multiphase fluid distributions* in porous media. For *simulating* multiphase flow inside a reconstructed porous structure it is important to find the geometrical regions occupied by the different fluids inside the porous space. Specifically, for two-phase flow it is important to geometrically locate the wetting and non-wetting phases inside the porous space at a given time.

Conceived as a dynamical problem, two-phase fluid invasion into a porous structure is complicated due to the difficulty in predicting the location of the interface between the two fluids as it is the site of dynamical unstability sources, considering the competition between inertial forces, surface tension and viscous transfer of momentum. In the present work, two-phase fluid invasion is supposed to proceed following a sequence of quasi-static processes between equilibrium states. The dynamic invasion problem is, thus, strongly simplified and reduced to the determination of the interface between the two fluids by using the well-known Young–Laplace equation. In fact, Young–Laplace equation predicts a *constant curvature* for an interface in mechanical equilibrium. The location of the interface can, thus, be regarded as a *geometrical problem*.

The purpose of this work is to present a methodology for determining this interface, considering two immiscible phases inside a 3D porous space, at a given equilibrium state. The work is limited to the study of mechanical equilibrium: mass transfer between the phases is not considered. The method is based on a 3D extension of the opening method from image analysis. From the authors' knowledge, this idea was firstly used in the study of water vapour sorption in two-dimensional porous sections by Quenard and Bentz (1992), although Delfiner et al. (1972) were the first to propose the use of opening methods, in the simulation of mercury intrusion. Recently, Yao et al. (1997) have used this method for studying mercury intrusion into 3D porous structures reconstructed from the data obtained from Vosges sandstone.

The great advantage of the presently proposed methodology with respect to percolation networks conception that simplifying assumptions regarding the geometry of the porous space are avoided, as mentioned above. In fact, invasion of wetting fluid in imbibition and wetting fluid retention in the later stages of drainage occur spatially through a complex structure of corners and intrinsic irregularities of pore surfaces that are very difficult to model by using percolation networks of sites and bonds.

2. Geometrical problem

Consider a system, U, composed by a rigid porous sample, $M \subset U$ (Fig. 1). Let L be the free region between the porous sample and the walls T of system U, $L = U - M \cup T$. It is supposed that L is large enough as compared with porous cavities to ensure that this region is not the site of any important capillary process. In this manner, L is defined as a geometrical region whose boundary has a curvature radius $r_L \to \infty$. M is the union of the solid matrix, S, and the porous space P, $M = S \cup P$. It is supposed that both M and S remain invariant during any process. The constancy of M and S assures, respectively, that the porous body is macroscopically and microscopically rigid. Let F be the region in U which can be occupied by one or more fluids, i.e., $F = U - T \cup S$.

Consider an invasion process where a fluid B displaces a fluid A inside the porous space. It is supposed that the two fluids are immiscible and the present work is only concerned with quasi-static processes. Let this process be considered as a sequence (i, $i = 0,1, \ldots, p$) of elementary steps between equilibrium states. For each step i, B^i is the geometric region occupied by fluid B and, for step 0, B^0 is such that $B^0 \cap P = \phi$, i.e., the invader fluid is outside the porous body at the beginning of the process. For each step i, B^i is a connected geometrical region, while A^i is the union of several geometrical regions which became disconnected during

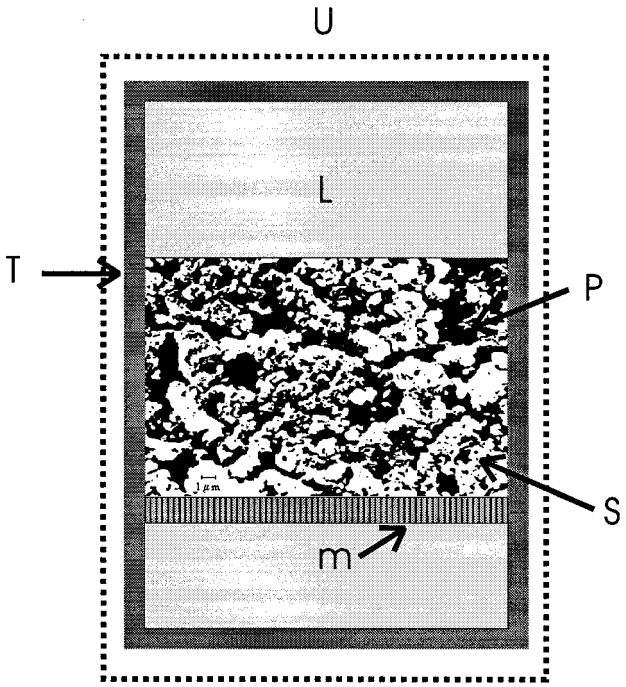

Fig. 1. Geometrical problem for fluid invasion into a porous structure M: solid (S), porous, (P) and free (L), regions are represented and, also, the wall (T). The region of fluids is $F = U - T \cup S$. A semi-permeable membrane (m) is also represented in the figure for preventing bubbling in the free region (L) in the course of the invasion process.

the invasion process. In fact,

$$A^i = A_0^i + \bigcup_{k=1}^{n(i)} A_k^i, \tag{1}$$

where, in step i, A_0^i is the geometrical partition of A which remains connected to the free region L during the invasion process and A_k^i, $k = 1, \ldots, n(i)$, is one of the $n(i)$ regions in F which became disconnect from L due to trapping by fluid B.

The trapped domain Y at step i is formally defined as

$$Y^i = A^i - A_0^i \quad 1 \leq i \leq p. \tag{2}$$

At step i of invasion, let E_x^i be a ball of radius r^i, centred at x, for a given point x belonging to region F, i.e., the union of the porous region, P, and the free region, L. Radius r^i is determined from the well known Young–Laplace equation, which establishes the equilibrium condition at the interface between fluids A and B,

$$r^i = \left| \frac{(d-1)\sigma_{AB}}{P_{A_0^i} - P_{B^i}} \right|, \tag{3}$$

where d is the Euclidian dimension of the space, σ_{AB} is the interfacial tension between fluids A and B, $P_{A_o^i}$ is the pressure at the domain of fluid A which is connected to the free region L, and P_{B^i} is the pressure of fluid B, at step i.

For points x that are closer than r^i from the boundary of F, the ball E_x^i will intercept this boundary. For this reason a new ball E_x^{*i} is defined such that,

$$E_x^{*i} = \begin{cases} E_x^i & \text{if } d_x \geq r^i \\ \phi & \text{if } d_x < r^i \end{cases}, \tag{4}$$

where d_x is the smallest of the distances between point x and the boundary of F.

An opening region H is defined such that at step i,

$$H^i = \bigcup_x E_x^{*i} \quad x \in F. \tag{5}$$

Here, H^i is a region whose interface has one of its two curvature radius constant and given by r^i. As it is the union of spherical balls enclosed in F, this interface makes a contact angle of 0° with the solid boundaries, defined with respect to the wetting phase.

For simulation purposes, the free region L is constructed with a boundary having a finite curvature radius. In this manner, a new opening region is defined as,

$$G^i = L \cup H^i. \tag{6}$$

It is important to define a complementary region of G^i, to find the phase distribution in the porous phase at step i, as

$$\underline{G}^i = F - G^i. \tag{7}$$

Fig. 2 represents the above defined regions for a two-dimensional (2D) porous body with a single cavity.

Let J and Q be any two regions of F and let $K(J, Q)$ be a union operator defined as the union of the connected components J_j of J with a non-null intersection with Q,

$$K(J,Q) = \bigcup_{k=1}^{n(J)} \begin{cases} J_j & \text{if } J_j \cap Q \neq \varnothing \\ \varnothing & \text{if } J_j \cap Q = \varnothing \end{cases}, \tag{8}$$

evidently,

$$K(K(J,Q),Q) = K(J,Q). \tag{9}$$

To illustrate the method Figs. 3 and 4 show an invasion process by, respectively, a wetting and a non-wetting fluid B, into a single 2D pore cavity, composed by two rectangular ducts P_1 and P_2 with different radii and arranged to show the effect of trapping. A membrane is placed at the wetting fluid side to maintain the pressure difference between the two phases and to prevent bubbling into the wetting fluid.

At the beginning of the wetting fluid invasion process, Fig. 3, consider that pressure difference $P_A - P_B$ is high enough to prevent wetting fluid invasion into the porous structure. Invasion will start when this pressure difference is decreased until Eq. (3) is satisfied for r^i equal to duct P_2 half-width. This first step is presented in Fig. 3(b), which shows the geometrical region inside the porous cavity where wetting fluid is considered to be, at this step. To *predict* this geometrical configuration at any given pressure step, present method starts by constructing the opening region G^i and its complementary region $\underline{G}^i$, using Eqs. (6) and (7),

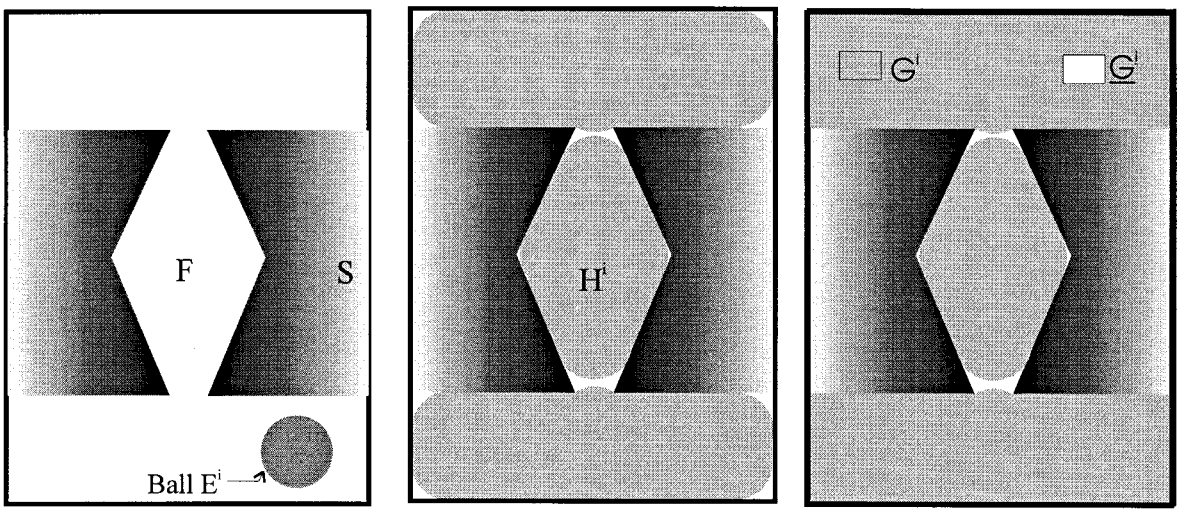

Fig. 2. The opening operation performed with a ball E_x^i splits region F into a convex region G^i and a complementary concave region $\underline{G}^i$.

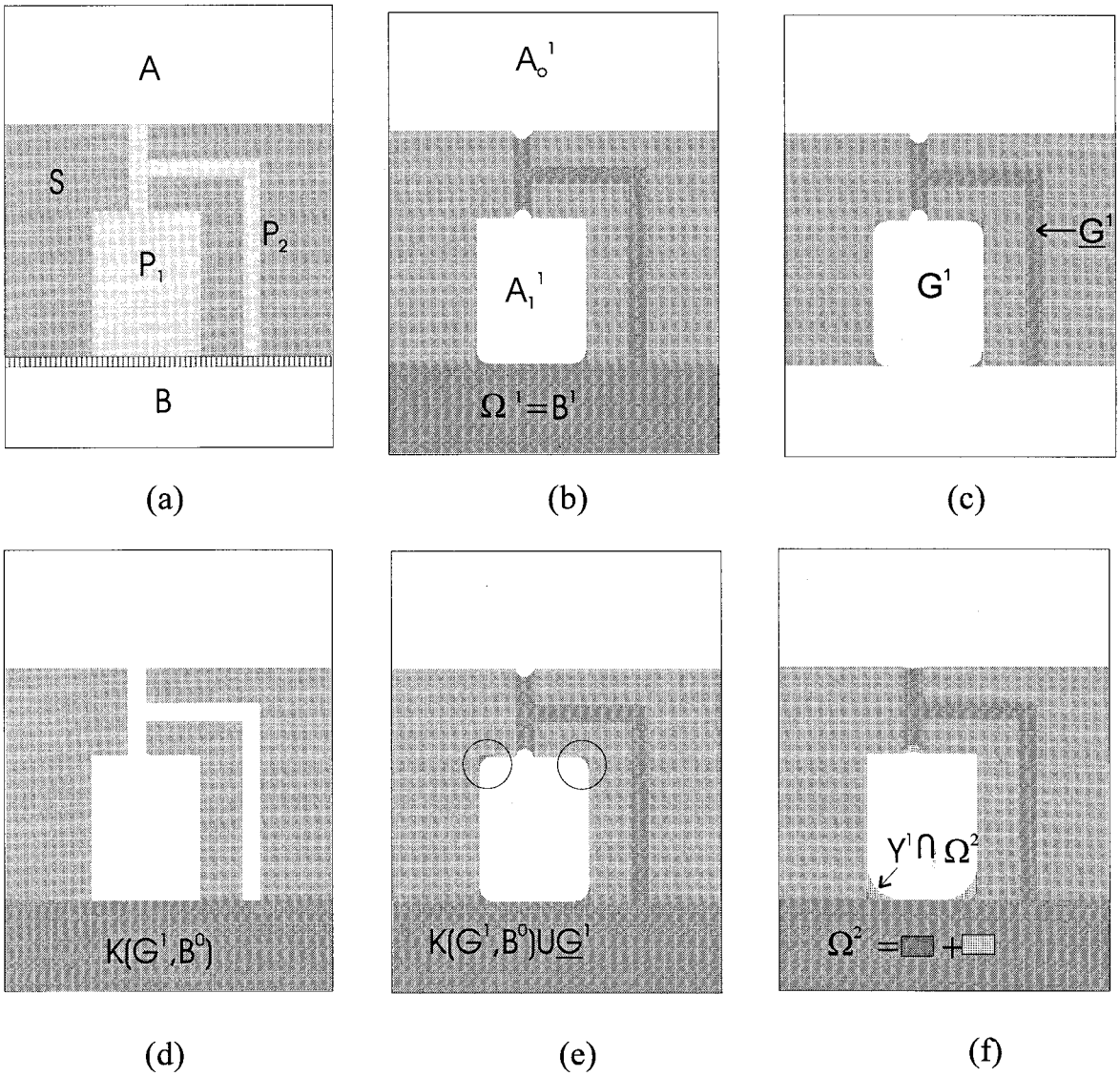

Fig. 3. Invasion of a sample pore cavity by a wetting fluid B. A semi-permeable membrane, shown schematically at (a). The equilibrium configuration B^1 is shown in (b) without the separation membrane. The opening region G^1 is shown with its complementary region $\underline{G}^1$ in (c), for a given radius r^1, corresponding to a first step of the invasion process. In (d) it is shown the union of the elements of G^1 having a non-null intersection with B^0, i.e., $K(G^1,B^0)$. Set $\Omega^1 = K\{[K(G^1,B^0) \cup \underline{G}^1],B^0\}$ is shown in (e). Encircled regions are isolated from the invading fluid and are eliminated with the application of the K operator. Regions Ω^2 and $\Omega^2 \cap Y^1$ at a second pressure step are shown in (f), when fluid A is considered to be incompressible.

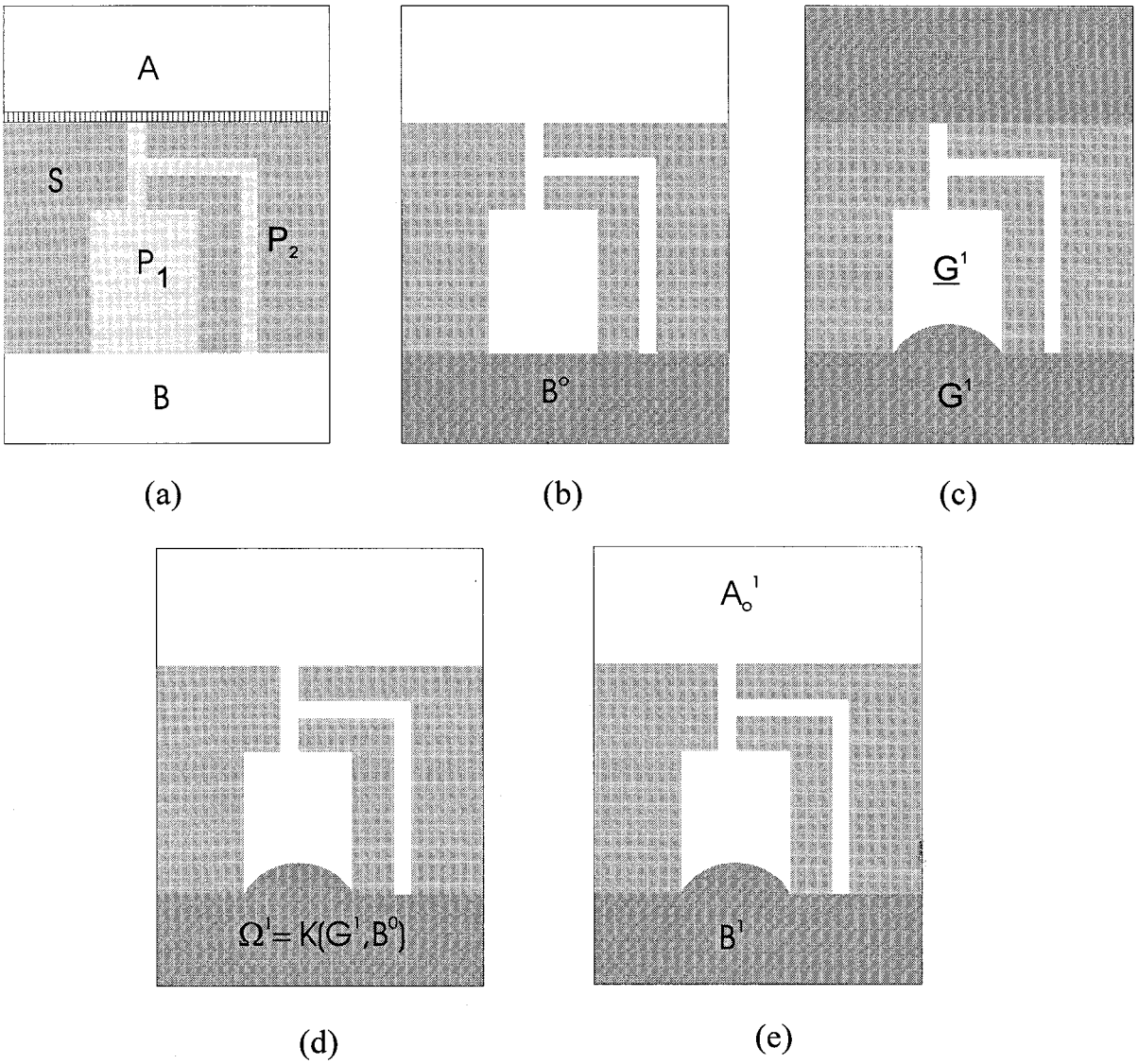

Fig. 4. Invasion of a sample pore cavity by a non wetting fluid B. A semi-permeable membrane is shown schematically in (a). Region B^0 is shown in (b) without the separation membrane. The opening region G^1 is shown with its complementary region $\underline{G}^1$ in (c), for a given radius r^1, corresponding to a first step of the invasion process. In (d) it is shown the union of the elements of G^1 having a non-null intersection with B^0, i.e., $K(G^1,B^0)$ which is set Ω^1 when B is a non-wetting fluid. The invaded region B^1 after the first step is shown in (e). In this sample case $B^1 = \Omega^1$ as there is no trapping.

with a ball radius given by Eq. (3). Fig. 3(c) presents these two regions, at step 1. Fig. 3(d) shows the result of the application of the union operator K defined in Eq. (8) to the connected components of G^1 with a non-null intersection with B^0, $K(G^1,B^0)$, shown in Fig. 3(c). In this sample case G is composed by three components: chamber A, almost the whole duct P_1 and

chamber B. In this manner $K(G^1,B^0)$ is simply B^0. To find the region occupied by fluid B at step 1, $K(G^1,B^0)\cup\underline{G}^1$ is calculated (Fig. 3(f)). Nevertheless, this union operation brings together components which are isolated from B^0, shown in Fig. 3(e) as encircled regions. To eliminate these components the union operator K is applied a second time giving $\Omega^1 = K\{[K(G^1,B^0)\cup\underline{G}^1],B^0\}$: this results in the geometrical region filled by fluid B at step 1 and shown in Fig. 3(b). To proceed with the simulation the isothermal compressibility k_T of fluid A (and/or B) must be known. In present paper, fluids are considered either to be *ideally* compressible ($k_T\to\infty$) or to be *ideally* incompressible ($k_T = 0$). If fluid A is ideally compressible, invasion into duct P_1 will proceed and can be simulated in the same manner as above: in present sample case a pressure reduction in $P_A - P_B$ will increase the interface curvature radius until the pressure difference satisfies Eq. (3) for r^i equal to duct P_1 half-width, when this duct will be fully occupied by fluid B. If fluid A is ideally incompressible, the geometrical configuration of the trapped regions, such as $Y^1 = A_1^1$ in Fig. 3(b), will remain unchanged during the remaining part of the invasion process. Considering a further step 2, the union operator K will produce the region Ω^2 shown in Fig. 3(f), which includes a part of the trapped region Y^1, equal to $\Omega^2\cap Y^1$. To find the geometrical region filled by fluid B^2 at step 2, region $\Omega^2\cap Y^1$ must be subtracted from Ω^2. Using $M - N \equiv \{x\in U; x\in M \text{ and } x\notin N\}$, for any two sets M and N, region B^2 can be found by calculating $\Omega^2 - \Omega^2\cap Y^1$ (or, which is the same: $\Omega^2 - Y^1$, since B^2 must exclude *any* component of the trapped region Y^1). Although not shown in the sample invasion process of Fig. 3, it must be observed that to find region B^i, at step i, it is necessary to subtract Y^i, rather than Y^{i-1}, from Ω^i, to, also, exclude the fluid which has invaded *dead ends* of the porous structure, in the steps $i-1$ to i. This is necessary since the presence of an ideally non-compressible fluid, filling a dead end and blocked by the wetting fluid, will prevent further invasion into this geometrical region. Region A^2 is then calculated from B^2, using $A^2 = F - B^2$, and the method follows, recursively, for the next pressure steps.

Fig. 4 illustrates an invasion process by a non-wetting fluid in the same 2D porous cavity, as in Fig. 3. At the beginning of the process, pressures P_A and P_B are equal. Non-wetting fluid invasion is produced by increasing P_B with respect to P_A and a first step is shown in Fig. 4(e), when fluid B has invaded a part of the porous cavity. Simulation is performed by decreasing r^i, in accordance with Eq. (3), when $P_B - P_A$ is increased. For a given pressure step i, the opening region G^i and its complementary $\underline{G}^i$ are calculated in, exactly the same way as above. This is shown in Fig. 4(c) for step 1. For non-wetting invasion, region Ω^1 can be calculated directly from the union operator $K(G^1,B^0)$ as shown in Fig. 4(d), which is, in this sample case, the geometrical region B^1 which is to be predicted at this step.

For each step i, the above exposed procedures can be generalised. For a set $\aleph$, defining $a\aleph$ to be $\aleph$ when $a = 1$ and to be the null set $\varnothing$ when $a = 0$, the geometrical region occupied by fluid B can be determined using the following equation:

$$B^i = \Omega^i - u_A Y^i, \tag{10}$$

where

$$\Omega^i = K\{[(W_B)\underline{G}^i\cup K(G^i,B^0)],B^0\}, \tag{11}$$

and W_B is a wetting factor for fluid B ($W_B = 1$, when fluid B is the wetting fluid and $W_B = 0$

otherwise), u_A is a compressibility factor for fluid A ($u_A = 0$ for fluids which are ideally compressible and $u_A = 1$, for fluids which are ideally incompressible). When fluid A is incompressible, domain B at step i is, thus, dependent, on the trapped domain Y^i, which is not known at this step. In present work, domain Y^i is approximated by the geometrical region that is trapped at step $i-1$, $Y^i \approx Y^{i-1} = A^{i-1} - A_0^{i-1}$. The degree of approximation will be, therefore, dependent on the step extent between two consecutive equilibrium states. In a 3D discrete representation of the porous microstructure, this means, by Eq. (3), that reliability of present simulation model, will be dependent on voxel linear dimension.

The above exposed method is, also, approximated in the sense that, in 3D the external surface associated with the union of balls with a given radius r does not have a curvature radius equal to $r/2$ (see Eq. (3)). This radius is not constant, depending on the porous surface curvature. In consequence, the predicted interface does not, rigorously, obey the Young–Laplace equation. Nevertheless, this deviation is expected to be small, excepting in the cavities where the porous surface has curvature radii with a very large aspect ratio. Considering, e.g., the question of determining the true location of the interface for wetting fluid invasion through the corners of a prismatic shape cavity with a rectangular cross section, the proposed model would predict an interface closer to the corner. Another source of deviation is related to the contact angle, exposed below.

2.1. Contact angle

Let θ_{AB} be the contact angle defined, as usually, with respect to the wetting fluid. As invasion is quasi-static it is supposed that θ_{AB} remains constant during the invasion process. The proposed solution given by Eqs. (10) and (11) results in equilibrium configurations whose interface has a 0° contact angle.

For preserving the contact angle θ_{AB}, the ball $E_x^* i$ defined in Eq. (4) could be written such that

$$E_x^* i = \begin{cases} E_x^i & \text{if } d_x \geq r^i \cos\theta_{AB} \\ \varnothing & \text{if } d_x < r^i \cos\theta_{AB} \end{cases}. \tag{12}$$

As it is shown in Fig. 5 it is however necessary, in this case, to consider in each ball E_x^{*i}, the region of the ball contained in region F. This can be done by neglecting the points which belongs to $E_x^{*i} \cap S$. This procedure is, however, processing time expensive. It is, also, very difficult to solve some computational problems associated with this procedure, as illustrated in Fig. 6. In this figure it is simulated an invasion process by a non-wetting fluid in a geometrical restriction between three spheres of different diameter. At step i, for a given pressure p^i of the non-wetting fluid it is associated a ball radius r^i. Fig. 6(a) shows where would be the interface of the non-wetting fluid, as calculated using Eq. (12), while Fig. 6(b) shows the correct interface. In fact, a non-wetting fluid is not able to penetrate through the restrictions shown in the figure, when the capillary pressure has a value related to r^i, although it is not, apparently, possible from a computational point of view to prevent solutions like the one shown in Fig. 6(a), using Eq. (12). In Fig. 6(c) it is shown the zero contact angle approximation for the

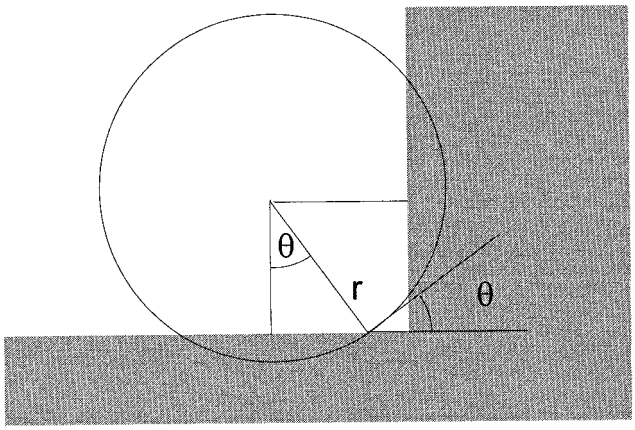

Fig. 5. Influence of contact angle

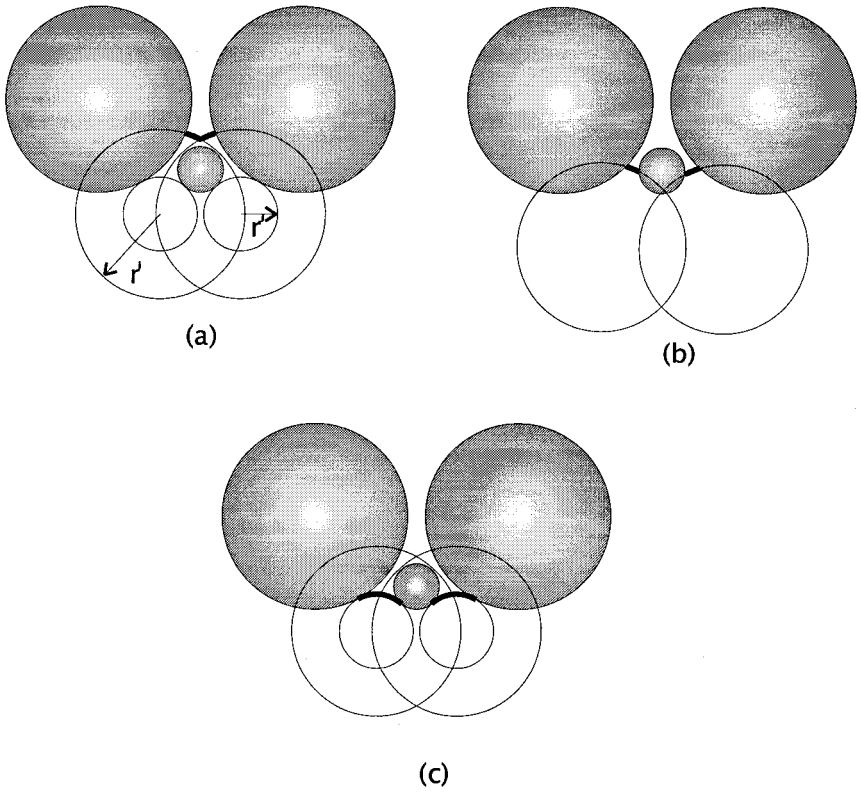

Fig. 6. Invasion process by a non-wetting fluid in a geometrical restriction between three spheres of different diameter. In (a) it is shown where would be the interface of the non-wetting fluid, as calculated when using Eq. (12), while in (b), it is seen the correct interface. In (c) it is shown the zero contact angle approximation for the interface.

interface, used in the present work, at step j. Invasion inside the restrictions will only occur at a farther step j corresponding to a lower ball radius r^j.

To take account of this effect, the ball radius r^i at each pressure step Δp^i is calculated in present zero contact angle approximation as in Eq. (3). In Fig. 6 the ball radius r^j will thus correspond to a non-wetting fluid pressure Δp^j corrected by $\cos\theta_{AB}$. As it is shown in the above example, this is, apparently, a better approximation as compared with the use of Eq. (12) and has been adopted in the present work.

3. Simulation procedure

Computational procedure starts from a 3D phase function $Z(\mathbf{r})$ whose domain is a cube, representing the system to be analysed, including the porous material and the chambers where the wetting and non-wetting fluid are to be placed, for simulation purposes. $Z(\mathbf{r}) = 0$ if $\mathbf{r} \in \mathbf{S} \cup T$ and $Z(\mathbf{r}) = 1$ if $\mathbf{r} \in F$. In the first step, the distance d_x, defined in Eq. (4) is determined for each $\mathbf{r} \in F$. Distance d_x is the smallest of the distances from point $\mathbf{r} \in F$ to the boundary between region F and solid phases and will be, in the following text, called background distance (BD).

For a 3D system, $\mathbf{r}$ is a discrete variable and each $\mathbf{r}$ is associated to a given 3D cell in space. Using an Euclidean metric, and considering the distance between the centres of two adjacent cells as unitary, the distance between two adjacent cells with a common edge will be $\sqrt{2}$ and $\sqrt{3}$ when they have a common corner.

When three arbitrary cells a, b and c have their centres sequentially *aligned* and when the distances between cells, a and b, to a given cell 0 are known, it is easy to show that the squared distance between cells c and 0 can be written in terms of the first two, as:

$$d_{c0}^2 = 2d_{b0}^2 - d_{a0}^2 + 2d_{ab}^2. \tag{13}$$

To find the squared distance of each cell to the background (SBD), a corner is chosen as the starting point, and the cells of the first plane, $z = 0$, are labelled. In the next z planes, distance is calculated using Eq. (13). The procedure is sequential, following the 0–x, 0–y and 0–z directions, sequentially. Cells in the solid phase are labelled with 0, and the first cells in phase F, with a face, an edge or a corner adjacent to the solid phase are labelled with 1, 2 or 3, respectively. Squared distances can be stored in a ordinary computer as integers, using a 2 bytes address, instead of 4 bytes, necessary for real variables.

Matrix SBD (x, y, z) is important to find the several geometrical regions defined in Section 2. In this way, the opening region H^i, defined in Eq. (5), is obtained at step i, by placing a ball of radius r^i centred at each cell with a SDB, satisfying

$$(r^i)^2 < \mathrm{SDB} \leq \left(r^i + 1\right)^2, \tag{14}$$

and by considering all cells with $\mathrm{SBD} \geq (r^i + 1)^2$ as belonging to H^i. In fact, balls with radius r^i centred on cells with $\mathrm{SBD} \leq (r^i)^2$ intercept the boundary of phase F and cells with $\mathrm{SBD} \geq (r^i + 1)^2$ are always surrounded by cells with $\mathrm{SBD} \geq (r^i)^2$. Region G^i as its complement $\underline{G}^i$ can be then determined by using Eqs. (6) and (7).

4. Results

The above procedure was used to simulate mercury intrusion and wetting/non-wetting fluid invasion into a 3D reconstructed porous structure.

4.1. Three-dimensional geometrical reconstruction

Several methods exist to generate discrete random fields. Adler et al. (1990) and Fernandes (1994) generated isotropic media by a simplified version of an algorithm presented by Quiblier (1984) for general 3D porous media based on the truncated gaussian method. This algorithm was itself an extension of a 2D scheme devised by Joshi (1974). Here it is used the truncated gaussian method by applying Fourier transform, as proposed by Liang et al. (1998).

The method consists in generating a random function $Z(\mathbf{x})$ that is equal to zero in the solid phase and one in the pore phase and which verify the two average properties. Porosity is a given positive number smaller than 1. Normalised auto-covariance function $R_z(\mathbf{u})$ is a given function of $\mathbf{u}$ that verifies the general properties of a correlation function for the phase function $Z(\mathbf{x})$ but is, otherwise, arbitrary. The analysis is restricted to homogeneous media, where the statistical characteristics are assumed to be independent of position $\mathbf{x}$ in space. Due to homogeneity, porosity is a constant and $R_z(\mathbf{u})$ depends only on the vector $\mathbf{u}$. Moreover, when the porous medium is isotropic, R_z is a function only of $u = |\mathbf{u}|$, and does not depend on the direction of $\mathbf{u}$, i.e., $R_z(\mathbf{u}) = R_{\mathbf{z}}(u)$.

A random and discrete field $Z(\mathbf{x})$ can be devised from an independent gaussian field $X(\mathbf{x})$ when the latter is successively passed through a linear and a non-linear filter. The random variable $X(\mathbf{x})$ are assumed to be normally distributed with a mean equal to zero and a variance equal to one. The variables are non-correlated. A linear operator can be defined by an array of coefficients $a(\mathbf{u})$, where $\mathbf{u}$ belongs to a finite cube $[0, \mathrm{Lc}]^3$ in Z^3. Outside this cube, $a(\mathbf{u})$ is equal to zero. A new random field $Y(\mathbf{x})$ can be expressed as a linear combination of the random variable $X(\mathbf{x})$. The difficulty related to the above linear filter is to get $a(\mathbf{u})$ by solving a non-linear system of equations. Adler (1992) proposed a version using Fourier transform. From a computational point of view, the use of fast Fourier transform algorithm, instead of laborious solution of non-linear equations, makes Fourier transform method superior to the above method. Application of Fourier transform is, however, restricted by resident memory requirements. To overcome those problems, an existence theorem, Papoulis (1965), provides an alternative method for generating normal fields. Given a positive-definite function $R_Y(\mathbf{u})$, it is possible to find a stochastic process $Y(\mathbf{x})$ having $R_Y(\mathbf{u})$ as its normalised auto-covariance function. By definition of Fourier transform and the Wiener–Khinchin theorem, the Fourier transform of the correlation function of a field is also its power spectrum. Therefore, if the correlation function of an arbitrary field is known, one can use Fourier transform to generate this field $Y(\mathbf{x})$ with the same auto-covariance function (Pardo-Igúzquiza and Chica-Olmo, 1993). The difference between this method and previous ones is that $Y(\mathbf{x})$ is directly generated from its auto-correlation function $C(\mathbf{u})$, and does not need the linear filter transform $X(\mathbf{x}) \rightarrow Y(\mathbf{x})$. In addition, when compared with Adler's method (Adler, 1992), Liang et al.'s (1998) method reduces the resident memory requirements, because the independent gaussian field data $X(\mathbf{x})$ are not needed. These relations can be shown in Fig. 7. In this way, one first

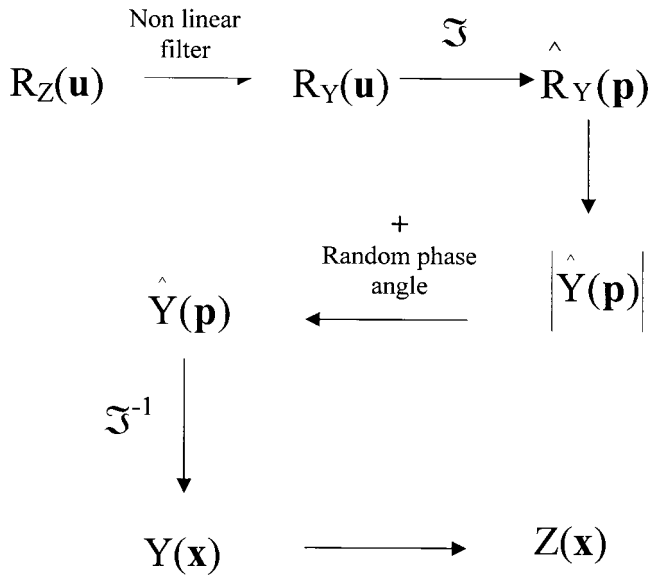

Fig. 7. Basic relations among stochastic process, correlation function, power spectrum and Fourier spectrum.

generates the Gauss field $Y(\mathbf{x})$ directly from its auto-covariance function, then use the truncated method to generate $Z(\mathbf{x})$.

Fig. 8 shows a binary representation of a polished thin section of the sample material, a Berea sandstone with a nominal permeability of 500 mD. Pores are shown in black and solid

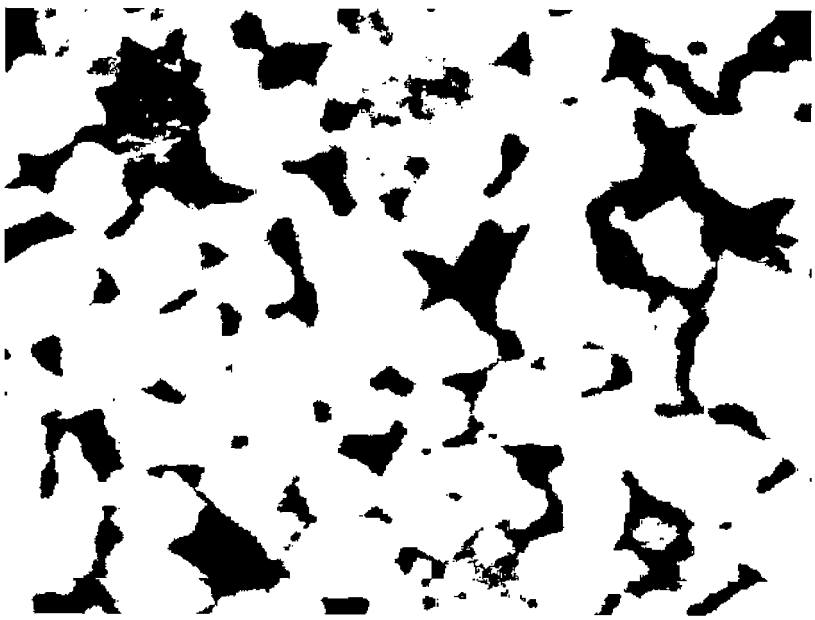

Fig. 8. Binary image of a polished thin section of a 500 mD Berea sandstone.

matrix in white. Each pixel corresponds to a square section of 2.6 μm^2 and the complete image has 609×458 pixels.

Three-dimensional reconstruction needs information about porosity ε and auto-correlation function $C(\mathbf{u})$. Considering isotropic sections, auto-correlation function is, usually, calculated along a given direction by displacing the binary representation over itself in the x direction (or y), using multiples of the pixel dimension and measuring the void fraction related to the intersection, i.e., the frequency of outcomes corresponding to two superposed black pixels (Adler, 1992; Philippi et al. 1994). Due to the finite size of this *discrete* binary representation with respect to pixel dimension, this above described procedure produces, generally, fluctuations on auto-correlation function. Since auto-correlation function $C(u)$ is related to the *probability* of finding two points separated by u and belonging to the same phase, it is advantageous to calculate $C(\mathbf{u})$ as a function of the 2D vector $\mathbf{u} = (x,y)$ and, then, to take its mean value around a circle with radius $u = |\mathbf{u}|$. This last procedure produces more reliable $C(u)$ values since it increases the number of realisations needed to calculate this probability.

The utilisation of presently well known and largely diffused fast algorithms, makes Fourier transform a very suitable tool to calculate $C(\mathbf{u})$, as a function of the displacement vector $\mathbf{u} = (x,y)$. Using Wiener–Khinchin theorem, normalised auto-covariance function $R_Z(\mathbf{u})$ was measured by calculating the power spectrum of the phase function $Z(\mathbf{x})$, i.e.,

$$R_Z(\mathbf{u}) = \Im^{-1}\left|\hat{Z}(\mathbf{p})\right|^2, \tag{15}$$

where $\hat{Z}(\mathbf{p})$ implies the direct Fourier transform of $Z(\mathbf{u})$ and $\Im^{-1}$ is used to indicate the corresponding inverse operation. Taking the mean value of R_Z for the several $\mathbf{u}$ with the same norm produces $R_Z(u)$, used in the present work to 3D geometrical reconstruction of the porous structure.

Fig. 9 shows a comparison between the above described methods for calculating the auto-correlation function $C(u)$ for the sample image, Fig. 8.

Fig. 10 shows a 3D view of the reconstructed microstructure for a given realisation.

Fig. 11(a) shows a comparison for the cumulative porous volume fraction measured on the original binary image and on several 2D cross sections of the reconstructed microstructure. These curves were obtained by measuring the cumulative area fraction on several 2D serial cross sections sliced from the reconstructed 3D representation and by taking the average values between these sections, for a given pore radius. Opening operation from image analysis was used in this computation step (Chassery and Montanvert, 1991). Factor n is a sampling factor taken over $R_Z(u)$ data: sampling factor n means that the only points considered for $R_Z(u)$ data were the ones separated by $n-1$ pixels. Reconstruction was performed trying to preserve the 3D representation linear size, in microns and taking computer resident memory limitations into account. In fact, resident memory requirements increase by a factor 2^3 when sampling factor n is halved, for the same linear size in microns. Factor N gives the linear size, in voxel, for each curve. In this manner, the linear size of all reconstructed cubes is 1040 μm, excepting curves $n = 6, N = 100, n = 2, N = 150$ and $n = 1, N = 200$, with linear sizes 1560, 780 and 520 μm, respectively. Letters a, b,... indicate stochastic simulations performed with different random seeds. It is apparent from Fig. 11(a) that, in the present case, a linear size of 1040 μm for the 3D stochastically generated representations is largely enough to avoid random seed effects.

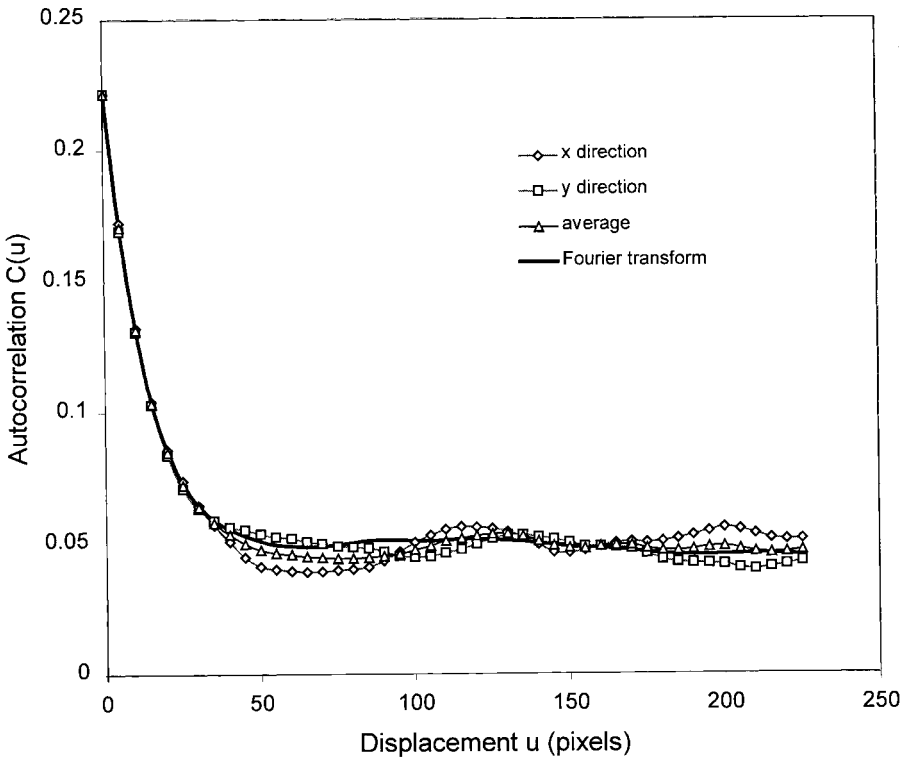

Fig. 9. A comparison between different methods for calculating the auto-correlation function $C(u)$ for the sample image, Fig. 8.

Results also show that, when sampling factor n is reduced, 3D reconstruction gives a systematic deviation with a larger amount of small-size pores when compared to the original binary image. The better agreement was obtained for $n = 6$ and $n = 4$. This is clearly seen in Fig. 11(b) which gives the pore size distribution, obtained as derivatives from the previous distribution curves. Although, due to computer storage limitations, it was not possible to generate refined 3D representations, with $n = 1$ and with the same linear size as the larger n ones, this systematic deviation is possible to be attributed to the reconstruction method itself, which appears to fail, when trying to preserve the size distribution of the smaller features found in the original 2D binary image. In fact, it must be remembered that present reconstruction method is based on: (i) the hypothesis that the original target 2D representation, Fig. 8, is a realization of a stochastic process which is considered to be ergodic and stationary and (ii) the hypothesis that this process is Gaussian and can be, inherently, described by its only first two moments.

4.2. Mercury intrusion

Mercury intrusion was simulated in 3D reconstructed porous structures of Berea sandstone. In a first system, intrusion was supposed to proceed through a single external surface of.a cube

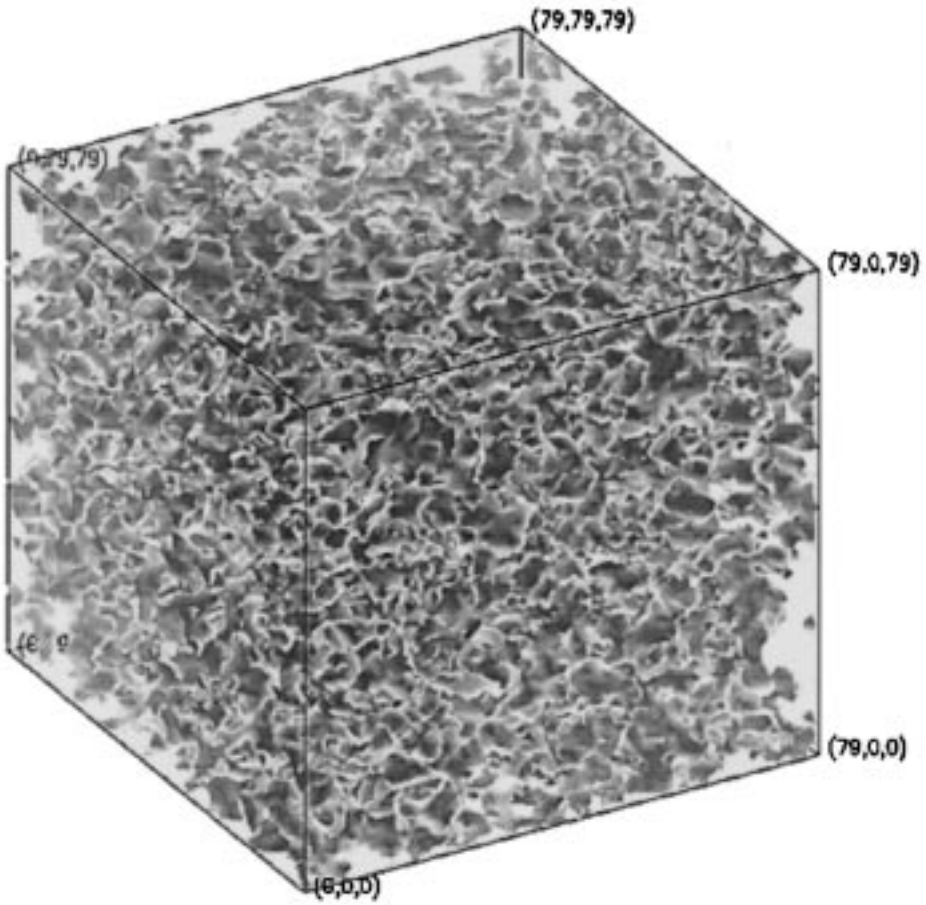

Fig. 10. Three dimensional view of the reconstructed microstructure of a 500 mD berea sandstone.

with size N^3 voxel. In a second system, intrusion was supposed to proceed through all the six external surfaces of the cube. For cubes with small sizes, surface effects due to mercury accommodation at the external boundary pores were more pronounced in system 2, although percolation was delayed in system 1. Considering that 3D reconstruction becomes, rapidly, hard to perform as the linear size N increases, due to the N^3 growing of computer resident memory requirements, results for larger samples, apparently indicate that both systems converge to the same results when the linear size is increased. Fig. 12 shows a set of previous results for the simulation of mercury intrusion: a comparison is performed between systems 1 and 2 for reconstructed cubes with sizes 100^3 and 150^3, respectively, using a sampling factor $n = 2$. In this figure $\alpha\beta$_Sγ indicates that simulation was performed on a β^3 voxel cube reconstructed with a random seed α, using system γ. In view of these previous results, system 1 was chosen for simulating purposes.

Fig. 13 shows a comparison between experimental values and system 1 simulation for mercury intrusion. Several reconstructed microstructures were used. Curves S_60N4T100,

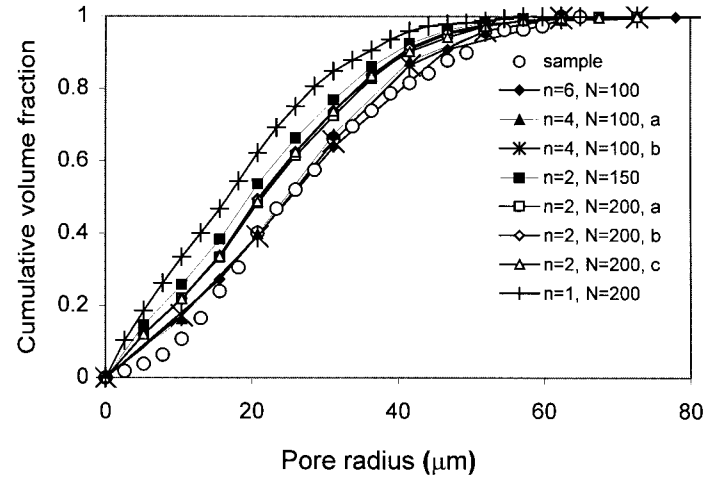

(a)

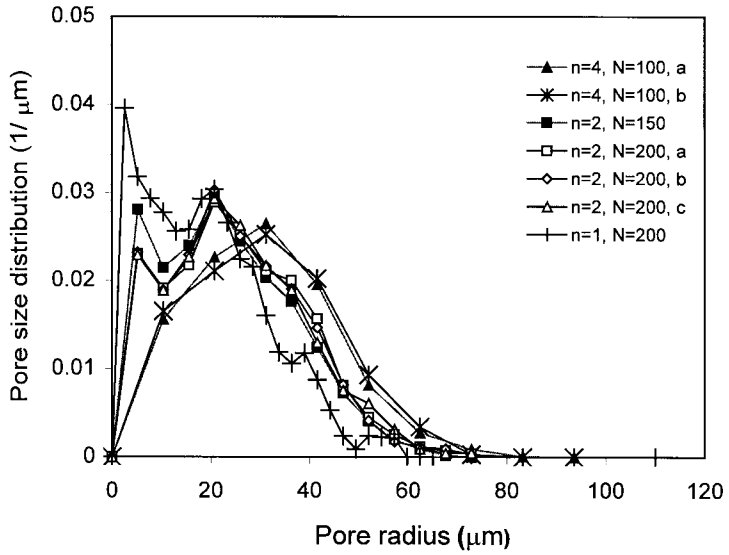

Fig. 11. (a) Comparison for the cumulative distribution of pore volume fraction between the values measured on the original binary image and the mean value obtained by measuring on several 2D cross sections of the reconstructed microstructure, (b) Pore size distribution obtained as derivatives of the cumulative volume fraction

S_80N4T100, S_100N4T100 represent the results of simulations on cubes with sizes 60^3, 80^3 and 100^3 voxel, respectively. All these cubes are pieces cut from a reconstructed microstructure with size 100^3 voxel, using a sampling factor $n = 4$. Curves S_150N2T150a and S_150N2T150b represent the results of simulation on 150^3 voxel cubes taken from two 3D representation reconstructed with 150^3 voxel, using a sampling factor $n = 2$ and different random seeds. Curves S_200N2T200a and S_200N2T200b represent the result of simulation on a 200^3 voxel 3D representation reconstructed with 200^3 voxel, using a sampling factor $n = 2$.

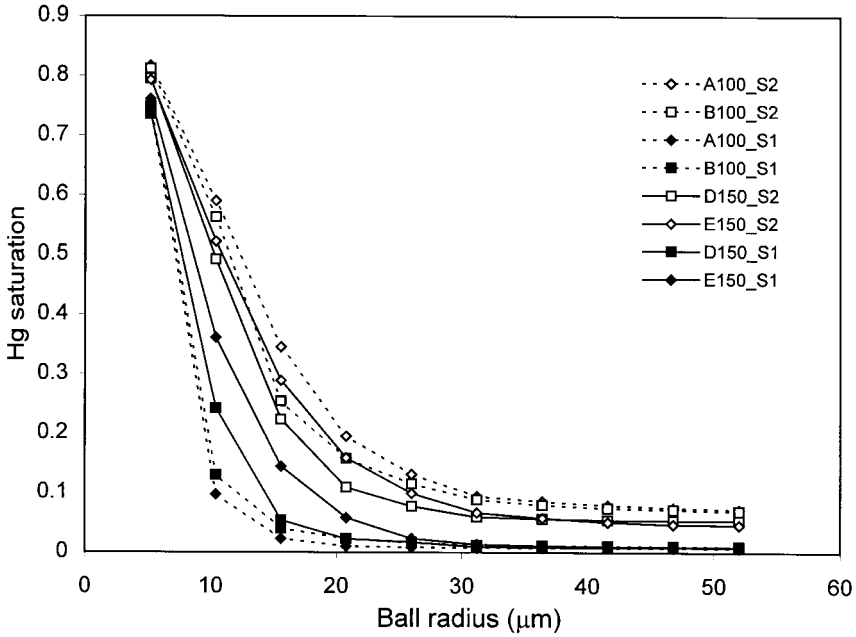

Fig. 12. A set of previous results for the simulation of mercury intrusion: a comparison is performed between systems 1 and 2 for reconstructed cubes with sizes 100^3 and 150^3, respectively, using a sampling factor $n = 2$;$\alpha\beta$_Sγ indicates that simulation was performed on a β^3 voxel cube reconstructed with a random seed α, using system γ

Measured values of intrusion pressures were converted to ball radius using Eq. (3), corrected by the cosine of the contact angle. Experimental values proceed from mercury intrusion experiments performed with large samples to avoid surface effects.

It is apparent from Fig. 13 that: (i) random seed in reconstructing the 3D representation has a very little influence on mercury intrusion simulation for linear sizes about 780 μm and above; (ii) although there is a good agreement between simulation and experimental results for 3D representations, with a sampling factor $n = 4$, percolation is retarded when simulation is performed on more detailed 3D representations, with $n = 2$. The above results and Fig. 11 indicate that retarded percolation on more detailed 3D representations is to be attributed to the larger amount of small-size pores obtained in 3D reconstruction when the sampling factor is reduced. These pores are distributed on the whole 3D porous structure representation, acting as constrictions and retarding mercury percolation.

4.3. Simulation of imbibition and drainage

Imbibition was simulated into a simple porous structure composed by some few identical solid spheres, randomly disposed inside a cubic shaped chamber. Results for two invasion steps are shown in Fig. 14. At each pressure step, porous structure was sliced in several parallel serial sections and Fig. 14 shows the geometrical configuration of the wetting (represented in blue colour) and non-wetting phases (in dark grey) corresponding to the first five serial sections, at that step. The first section represents the solid wall of the chamber and, the next

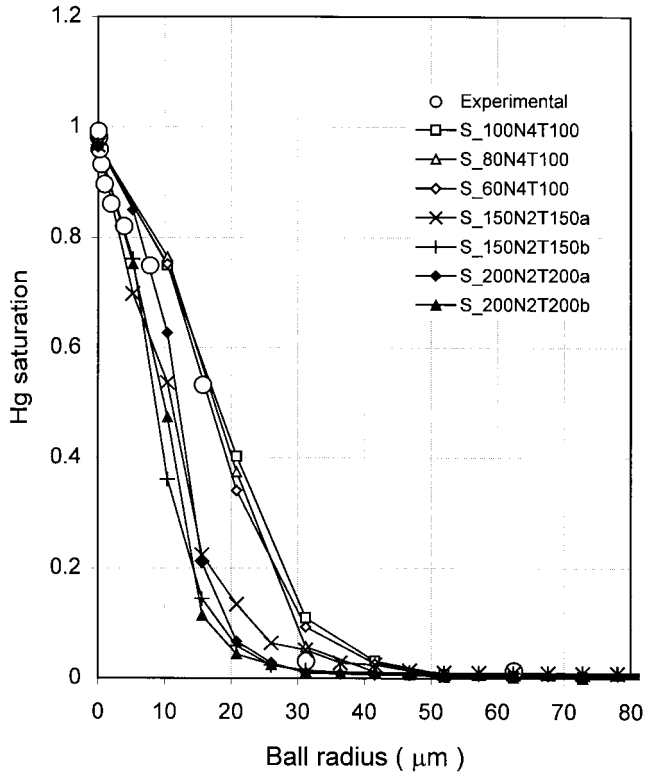

Fig. 13. Comparison between experimental values and system 1 simulation for mercury intrusion. S_αNβT$\gamma\delta$ indicates that simulation was performed on a α^3 voxel cube obtained from a γ^3 voxel reconstructed cube using a sampling factor $n = \beta$ and random seed δ.

ones, the pore structure between the solid spheres. It is clearly seen that, by increasing capillary pressure, invasion of the wetting fluid is adequately modelled, proceeding through the corners and smaller pores of the porous structure, as in regions 1 and 3, and producing blockage of the non-wetting fluid (represented in light grey as in region 2). These effects are very important in wetting-fluid invasion and entirely justified from a physical point of view. They cannot be predicted by, e.g., percolation networks, although several attempts have been made in the last few years for taking account of edge invasion, by the use of networks with square cross sections bonds, connecting cubic sites (Ioannidis and Chatzis, 1993c). In fact, the extreme irregularity of the porous surface produces a very complex network of 3D bonds for wetting-fluid invasion, which is very difficult to model by using percolation networks. In the present conception, corner invasion is an intrinsic consequence of the method used to predict the geometrical regions occupied by the wetting and non-wetting phases, inside the pore space. Corner invasion results in non-wetting fluid blockage, which can be fully appreciated in region 5, in the figure. In region 4, the centre of curvature of fluid interface is apparently inside the wetting fluid region. However, it must be observed that the interface is 3D and spatial composition of the several serial sections results in an interface with a centre of curvature inside the non-wetting phase.

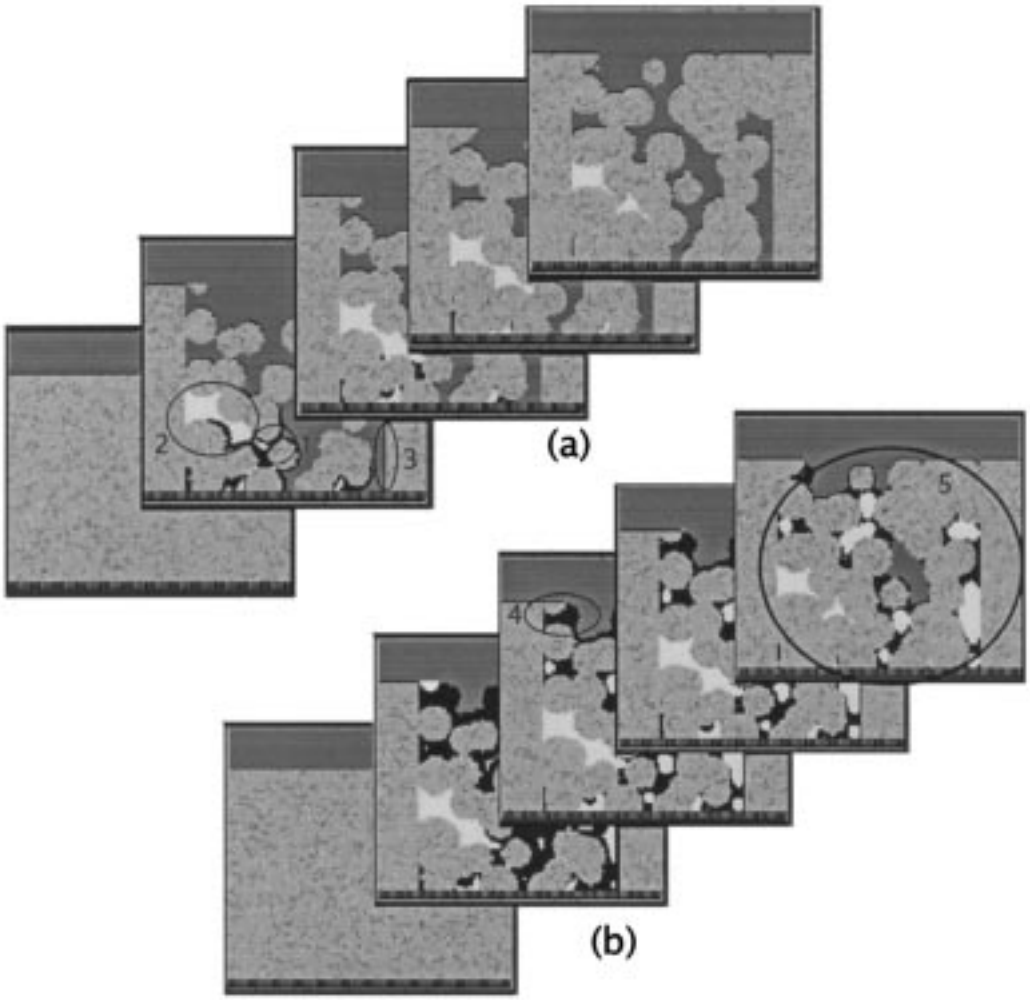

Fig. 14. Simulation of imbibition into a a simple porous structure composed by some few identical solid spheres, randomly disposed inside a cubic shaped chamber

Fig. 15 shows simulation results representing wetting fluid invasion into a Berea sandstone 3D reconstructed porous structure with 150^3 voxel and sampling factor $n = 2$. Curves A, B and C represents simulation for three different reconstructed cubes using different random generator seeds. Wetting and non-wetting fluids were considered as ideally non-compressible. Imbibition starts from point I1. For this point, interface between wetting and non-wetting fluids was found using a unitary radius ball (in voxel). Using Eq. (3) this radius can be converted to the smallest capillary pressure which was possible to predict in an imbibition process, starting from the original image resolution and considering the sampling factor n used in reconstructing the microstructure. At point I1 saturation was calculated as about 0.005. Points I2 were obtained with the next ball radius, corresponding to two voxel. As non-wetting fluid was considered to be non-compressible, wetting fluid invasion stops at I3 from which a

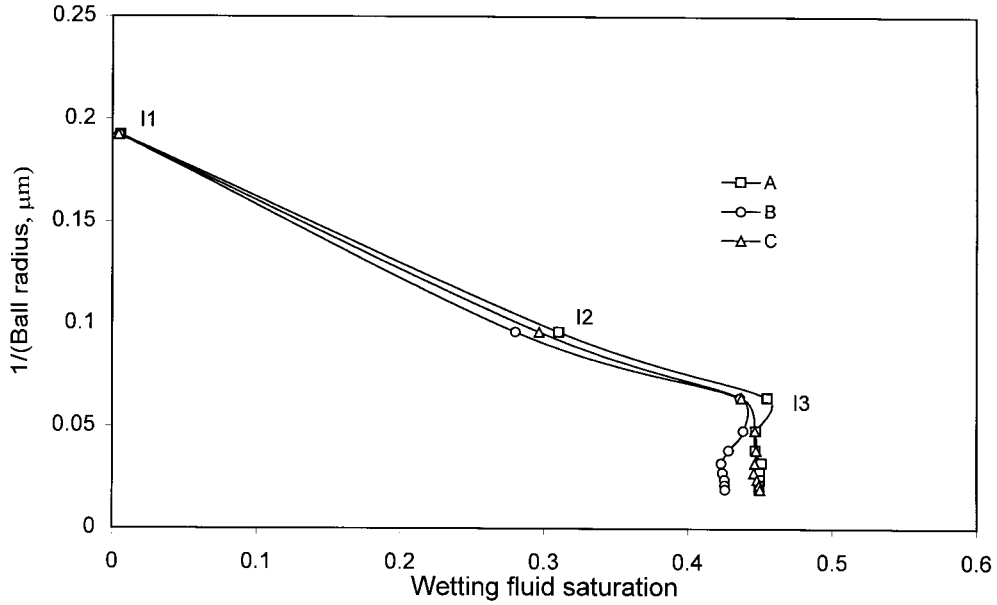

Fig. 15. Simulation of imbibition into a 150^3 3D reconstructed microstructure of a 500 mD Berea sandstone using a sampling factor $n = 2$. *A*, *B*, *C* correspond to three different random generator seeds.

later increase in capillary pressure produces no increase in wetting fluid saturation. In fact, from that point on the remaining non-wetting phase is completely blocked inside the porous space. The total amount of trapped non-wetting fluid was calculated as near 55% of the total porous volume, at this point. The small deviations presented at points I3, where wetting fluid saturation appears to diminish as capillary pressure increases, have no physical meaning and are to be considered as a deficiency of the method. Actually, this effect is very common in discrete morphology, where the objects to be analysed are sets of discrete points. As the wetting fluid region is considered to be the complementary set of the union of balls with a given radius and possible to be located inside the porous space, an increase in ball radius may produce a more complete filling of the porous space by this union of balls, reducing the amount available to the wetting fluid. This effect is more pronounced for reconstructed microstructure B.

Fig. 16 shows simulation results for drainage and comparison with experimental data for water and oil as, respectively, the wetting and non-wetting fluids. Simulation was performed using 100^3 voxel reconstructed microstructures of 500 mD Berea sandstone, with a sampling factor $n = 1$. Measured values, found in the literature and nearest to the simulated sandstone, were related to a 600 mD Berea and taken from Ioannids and Chatzis (1993c). Considering the lack of data for contact angle and interfacial tension related to the particular pair water–oil used in the experiments, curves were constructed using a reduced capillary pressure. Reduced capillary pressure is defined as $P_c^* = P_c/P_{c,th}$, where $P_{c,th}$ is the value of capillary pressure at threshold. Irreducible water saturation was found as 0.24, at the end of drainage. Evidently, the amount of trapped water at the end of drainage, found in simulations, is dependent on the

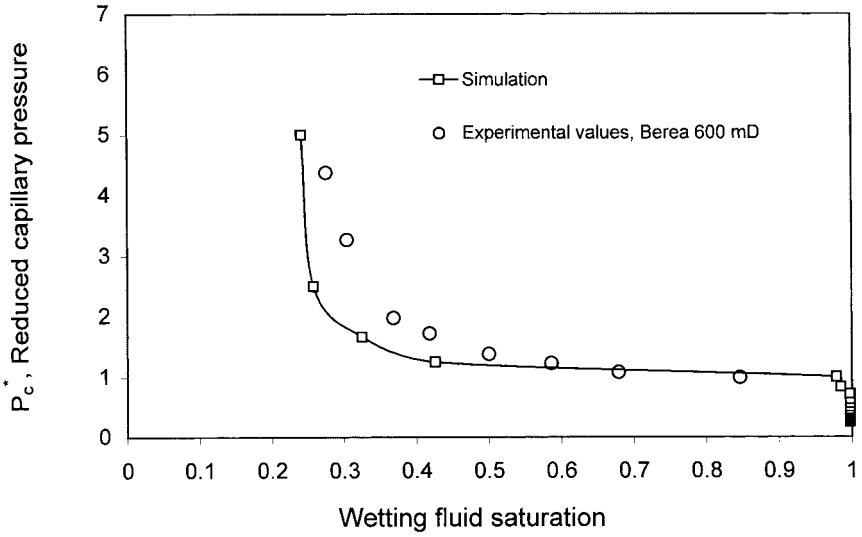

Fig. 16. Simulation of drainage for a 100^3 reconstructed microstructure of Berea sandstone, using a sampling factor $n = 1$ and comparison with experimental data.

final resolution and geometrical accuracy obtained for the original binary image used to reconstruct the porous microstructure. This must consider sample surface planarity, image acquisition process and software tools used for image segmentation and morphological filters. Nevertheless, simulation compares well with the experimental data at our disposal and restricted to P_c^* smaller than 5. Simulation for reduced capillary pressures greater than 5 would require image acquisition with a resolution higher than the presently used 1 pixel/2.6 μm^2.

It is interesting to compare the total amounts of displaced fluid at the end of imbibition and at the end of drainage, respectively, 45 and 76% of the porous volume. In the present work, this important difference is attributed to wetting fluid invasion by the corners and porous surface irregularities, in imbibition, as opposed to non-wetting fluid invasion in drainage, proceeding, mainly, by piston displacement along the inner axis of the porous space.

5. Conclusions

In present paper, a methodology was presented for studying two-phase equilibrium inside a porous medium, based on Young–Laplace's equation that predicts a constant curvature for the interface between two-phases in mechanical equilibrium. The great advantage of the presently proposed methodology with respect to percolation networks conception is that simplifying assumptions regarding the geometry of the porous space are avoided. The method is applied on 3D reconstructed porous structures.

Simulation of mercury intrusion and water–oil capillary curves are presented for Berea sandstone and compared with experimental data. Corner invasion and retention of wetting

fluid during the later stages of drainage are, apparently, adequately modelled, especially when compared with percolation networks models. Considering the limitations of the methodology, results, apparently, confirm its adequacy as a valuable tool for simulating two-phase equilibrium in porous media.

References

Adler, P.M., 1992. Porous Media: Geometry and Transports. Butterworth–Heinemann, New York.

Adler, P.M., Jacquin, C.G., Quiblier, J.A., 1990. Flow in simulated porous media. Int. J. Multiphase Flow 16, 691–712.

Chassery, J.M., Montanvert, A., 1991. Géométrie Discrete en Analyse d' Images. Hermès, Paris.

Chatzis, I., Dullien, F.A.L., 1982. Mise en oeuvre de la théorie de la percolation pour modéliser le drainage des mileux poreux et la peméabilité relative au liquide non mouillant injecté. Revue de L'Institut Français du Petrole 37, 183–205.

Daïan, J.F., Saliba, J., 1991. Determination d'un reseau aléatoire de pores pour modéliser la sorption et la migration d'humidite dans un mortier de ciment. Int. J. Heat and Mass Transfer 34, 2081–2096.

Delfiner, P., Étienne, J., Fonck, J.M., 1972. Application de l'Analyseur de Textures a l'Étude Morphologique des Réseaux Poreux em Lames Mices. Revue de l'Institut Français du Pétrole 27, 535–558.

Fernandes, C.P., 1994. Caracterização Morfotopológica de Espaços Porosos: Reconstituição Multi-Escala e Simulação de Processos de Invasão de Fluidos Não-Molhantes. Doctoral Thesis, Mechanical Engineering Department, Federal University of Santa Catarina, Florianópolis.

Hazlett, R.D., 1995. Simulation of capillary-dominated displacements in microtomographic images of reservior rocks. Transport in Porous Media 20, 21–35.

Ioannids, M.A., Chatzis, J., 1993a. The effect of spatial correlations on the accessibility characteristics of 3D cubic networks as related to drainage displacements in porous media. Water Res. Research 29, 1777–1785.

Ioannids, M.A., Chatzis, J., 1993b. A mixed-percolation model of capillary hysteresis and entrapment in mercury porosimetry. J. Coll. Int. Science 161, 278–291.

Ioannids, M.A., Chatzis, J., 1993c. Network modelling of pore structure and transport properties of porous media. Chem. Eng. Science 48, 951–972.

Ioannids, M.A., Kwiecien, M., Chatzis, I., 1995. Computer generation and application of 3D model porous media: from pore-level geostatistics to the estimation of formation factor. In: Paper SPE 30201 presented at the Petroleum Computer Conference, Houston, TX.

Joshi, M.Y., 1974. A class of stochastic models for porous media. Ph.D. thesis, University of Kansas, Lawrence, USA.

Koplik, J., Lin, C., Vermette, M., 1984. Conductivity and permeability from microgeometry. J Appl. Phys 56, 3127–3131.

Kwiecien, M.J., MacDonald, I.F., Dullien, F.A.L., 1990. Three-dimensional reconstruction of porous media from serial section data. Journal of Microscopy 159, 343–349.

Laurent, J.P., Frendo-Rosso, C., 1992. Application of image analysis to the estimation of AAC thermal conductivity. In: Wittman, F.H. (Ed.), Third RILEM Symposium on Autoclaved Aerated Concret, Zurich. A.A. Balkema, Rotterdam, p. 65.

Lenormand, R., 1981. Déplacents Polyphasiques en Milieux Porex sous l' Influence des Forces Capillaires-Etude Experimental et Modélisation de Type Percolation. Thèse de Doctorat d'Etat, Institut National Polytechnique de Toulouse, Toulouse.

Liang, Z.R., Fernandes, C.P., Magnani, F.S., Philippi, P.C., 1998. A reconstruction technique for 3D porous media using image analysis and Fourier transforms. J. Petroleum Science and Engineering 21, 273–283.

Mayagoitia, V., Javier Cruz, M., Rojas, F., 1989. Mechanist studies of capillary processes in porous media. J. Chem. Soc., Faraday Trans. I 85, 2071–2078.

Montemagno, C.D., Gray, W.G., 1995. Photoluminescent volumetric imaging: a technique for the exploration of multiphase flow and transport in porous media. Geoph. Res. Lett 22, 425–428.

Papoulis, A., 1965. Probability, Random Variables, and Stochastic Processes. McGraw-Hill, New York.

Pardo-Igúzquiza, E., Chica-Olmo, M., 1993. The fourier integral method: an efficient spectral method for simulation of random fields. Mathematical Geology 25, 177–217.

Philippi, P.C., Souza, H.A., 1995. Modelling moisture distribution and isothermal transfer in a heterogeneous porous material. Int. J. Multiphase Flow 21, 667–691.

Philippi, P.C., Yunes, P.R., Fernandes, C.P., Magnani, F.S., 1994. The microstructure of porous building materials: study of a cement and lime mortar. Transport in Porous Media 14, 219–245.

Pieritz, R.A., Philippi, P.C., 1995. The generalized median line graphics technique in porous media geometry characterisation. In: Proceedings of International Conference on Quality Control by Artificial Vision, Le Creusot, France, pp. 110–118.

Quenard, D.A., Bentz, D.P., 1992. Capillary condensation, hysteresis and image analysis. In: Proceedings of Drying'92 Symposium, pp. 253–262.

Quiblier, J.A., 1984. A new three-dimensional modelling technique for studying porous media. Journal of Colloid and Interface Science 98, 84–102.

Renault, P., 1991. The effect of spatially correlated blocking-up of some bonds or nodes of a network on the percolation threshold. Transport in Porous Media 6, 451–468.

Spanne, P., Thovert, J.F., Jacquin, C.J., Lindquist, W.B., Jones, K.W., Adler, P.M., 1994. Synchrotron computed microtomography of porous media: topology and transports. Phys. Rev. Lett 73, 2001–2004.

Thovert, J.F., Salles, J., Adler, P.M., 1993. Computerised characterisation of the geometry of real porous media: their discretisation, analysis and interpretation. J. Microscopy 170, 65–79.

Tsakiroglou, C.D., Payatakes, A.C., 1992. Effects of pore-size correlation on mercury porosimetry curves. J. Coll. Int. Science 146, 479–494.

Yao, J., Thovert, J.F., Adler, P.M., Tsakiroglou, C.D., Burganos, V.N., Payatakes, A.C., Moulu, J.C., Kalaydjian, F., 1997. Characterisation, reconstruction and transport properties of Vosges sandstones. Rev. Inst. Français du Pétrole 52, 03–21.